Title

Cell Architecture and Dynamics of Human Induced Pluripotent Stem Cell-Derived Cardiomyocytes (hiPSC-CMs) on Hydrogels with Spatially Patterned Laminin and N-Cadherin.

Journal

ACS Applied Materials & Interfaces, 17(1)

Authors

Lane, Kerry

Dow, Liam

Castillo, Erica

et al.

Publication Date

2025-01-08

DOI

10.1021/acsami.4c11934

Peer reviewed

ACS APPLIED MATERIALS & INTERFACES

www.acsami.org
Research Article

Cell Architecture and Dynamics of Human Induced Pluripotent Stem Cell-Derived Cardiomyocytes (hiPSC-CMs) on Hydrogels with Spatially Patterned Laminin and N-Cadherin

Kerry V. Lane,[▽] Liam P. Dow,[▽] Erica A. Castillo, Rémi Boros, Samuel D. Feinstein, Gaspard Pardon, and Beth L. Pruitt*

Cite This: *ACS Appl. Mater. Interfaces* 2025, 17, 174−186
Read Online

ACCESS | Metrics & More | Article Recommendations | Supporting Information

ABSTRACT: Controlling cellular shape with micropatterning extracellular matrix (ECM) proteins on hydrogels has been shown to improve the reproducibility of the cell structure, enhancing our ability to collect statistics on single-cell behaviors. Patterning methods have advanced efforts in developing human induced pluripotent stem cell-derived cardiomyocytes (hiPSC-CMs) as a promising human model for studies of the heart structure, function, and disease. Patterned single hiPSC-CMs have exhibited phenotypes closer to mature, primary CMs across several metrics, including sarcomere alignment and contractility, area and aspect ratio, and force production. Micropatterning of hiPSC-CM pairs has shown further improvement of hiPSC-CM contractility compared to patterning single cells, suggesting that CM−CM interactions improve hiPSC-CM function. However, whether patterning single hiPSC-CMs on a protein associated with CM−CM adhesion, like N-cadherin, can drive similar enhancement of the hiPSC-CM structure and function has not been tested. To address this, we developed a novel dual-protein patterning process featuring covalent binding of proteins at the hydrogel surface to ensure robust force transfer and force sensing. The patterns comprised rectangular laminin islands for attachment across the majority of the cell area, with N-cadherin "end caps" to imitate CM−CM adherens junctions. We used this method to geometrically control single-cell CMs on deformable hydrogels suitable for traction force microscopy (TFM) to observe cellular dynamics. We seeded α-actinin::GFP-tagged hiPSC-CMs on dual-protein patterned hydrogels and verified the interaction between hiPSC-CMs and N-cadherin end caps via immunofluorescent staining. We found that hiPSC-CMs on dual-protein patterns exhibited higher cell area and contractility in the direction of sarcomere organization than those on laminin-only patterns but no difference in sarcomere organization or total force production. This work demonstrates a method for covalent patterning of multiple proteins on polyacrylamide hydrogels for mechanobiological studies. However, we conclude that N-cadherin only modestly improves single-cell patterned hiPSC-CM models and is not sufficient to elicit increases in contractility observed in hiPSC-CM pairs.

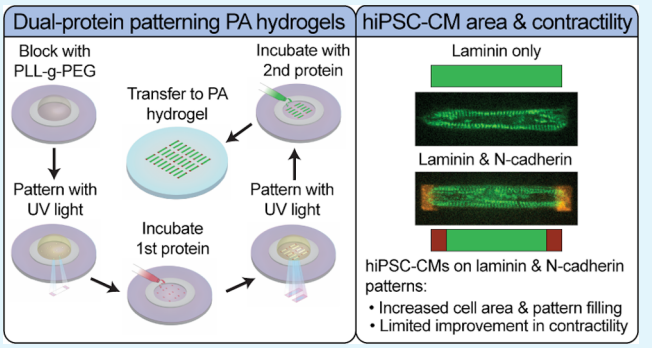

KEYWORDS: *protein micropatterning, hiPSC-CMs, single-cell cardiomyocytes, sarcomeres, contractility, N-cadherin*

INTRODUCTION

Human induced pluripotent stem cell-derived cardiomyocytes (hiPSC-CMs) are a promising model to bridge the gap between human heart function and studies using CMs from animal models.[1−4] Developments in CM differentiation protocols have expanded the use of hiPSC-CMs in research[5] and engineering interventions have helped overcome limitations to the use of hiPSC-CMs as models for primary human CMs. These limitations include differences in structure and function between hiPSC-CMs and adult human CMs, such as CM morphology, sarcomere organization, and contractile force.[4,6]

Single hiPSC-CMs are frequently used in studies that seek to investigate intracellular processes, including assessments of cardiotoxicity in preclinical drug studies, as an alternative to using primary CMs isolated from animal models.[7−10] For this reason, developing a better single-cell hiPSC-CM model would facilitate the use of human cells, a reduction in animals sacrificed for research, higher throughput drug screening assays, and lower costs, especially given the potential for massive expansion of hiPSC-CMs.[11]

Received: July 19, 2024
Revised: November 25, 2024
Accepted: November 25, 2024
Published: December 16, 2024

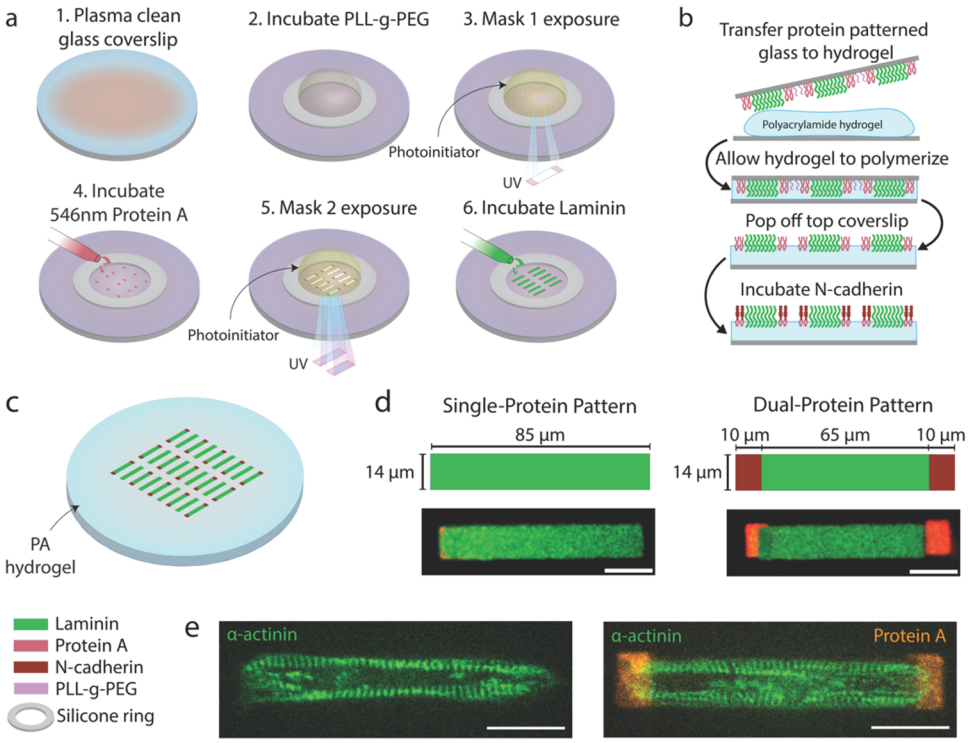

Figure 1. Dual-protein patterning of PA hydrogels. (a) Process flow of dual-protein patterning on a glass coverslip using photomolecular adsorption. (b) Process flow of transfer of dual-protein pattern from glass coverslip to PA hydrogel and incubation of N-cadherin. (c) Schematic of final result—alternating laminin-only and dual-protein patterns on PA hydrogel. (d) Schematics and representative images of fluorescently labeled laminin-only and dual-protein patterns on PA hydrogels. Green is laminin and red is N-cadherin. (e) Representative image of hiPSC-CMs on laminin-only (left) and dual-protein (right) patterns, with sarcomeres (green) and Protein A (orange) visible. Scale bars are 20 μm.

Our engineered single hiPSC-CM platform utilizes protein micropatterning with covalent attachment to hydrogels that mimic the mechanical properties of the myocardium; this platform improves the structure and function of hiPSC-CM for single-cell assays.[12−15] Protein micropatterning allows for the control of hiPSC-CM morphology by culturing the cells on rectangular ECM protein patterns in aspect ratios of 5:1 to 7:1, similar to the aspect ratio of adult human ventricular CMs.[1,14−16] Patterning hiPSC-CMs on deformable hydrogels better mimics the stiffness of the native environment and allows the CMs to fully contract, which is necessary for functional measurements such as traction force microscopy.[1,15,17] Patterned hiPSC-CMs present more highly aligned myofibrils and greater contractile forces within days of seeding on devices, and they mature these parameters much faster than unpatterned hiPSC-CMs.[15] With these single-cell hiPSC-CMs, we have a high degree of control over the microenvironment and can study sarcomere dynamics, and with the addition of fluorescent microbeads as fiducials in the deformable substrate, we can quantify contractile force dynamics.

Previous studies have investigated the effects of protein micropatterning on single-cell animal CMs and hiPSC-CMs, primarily focusing on the ECM proteins. Additionally, pairs of rat CMs have been micropatterned to control their shape and aspect ratio while providing for cell−cell contact.[18] These micropatterned CM pairs showed increased intracellular organization, force production, and contractility compared to single-cell patterned CMs.[18] We previously found a similar effect when patterning murine CMs, CM pairs generated more force per cell than single cells; and we also observed that the addition of externally applied stretch elicited a higher adaptive force output (consistent with the Frank-Starling relationship).[19] Taken together, these studies suggested to us that mimicking CM−CM interactions could further improve the maturity of single-cell patterned hiPSC-CMs.

N-cadherin is a key regulator of intercalated discs, the junctions mediating CM−CM interactions.[20] Previous studies have investigated the role of N-cadherin in the heart using single-cell, multicellular, and whole animal models from rats, mice, cats, and chicks.[21−23] These studies have demonstrated that N-cadherin plays a role in sarcomere organization and development, as well as myofibril stabilization and contraction.[21−23] Prior studies have also shown that N-cadherin-mediated mechanotransduction is distinct from ECM-mediated mechanotransduction.[24,25] These studies provided useful insight into the role of N-cadherin in CM development, function, and mechanotransduction,[20−25] however, they did not explore the interplay of N-cadherin and ECM proteins for single CMs; moreover, they used animal CMs, which have key physiological differences compared to human CMs.[26,27]

Here, we asked whether patterning both laminin (an ECM protein secreted by CMs and abundant in their native microenvironment) and N-cadherin improves the structure and function of single-cell hiPSC-CMs. To answer this, we developed a method for consistent and precise dual-protein patterning on deformable hydrogels, and tested the effects of these substrates on single-cell hiPSC-CMs. N-cadherin is a relatively short (130 kDa), asymmetric protein which requires rotational freedom for proper conformation and binding.[28] To ensure the covalent attachment of functional N-cadherin, we adapted a protocol from Sarker et al.[12] for the covalent attachment of Protein A as a linker to bind N-cadherin with an

https://doi.org/10.1021/acsami.4c11934
ACS Appl. Mater. Interfaces 2025, 17, 174−186

Fc-domain.[29] We used our protein micropatterning method to imitate both CM-ECM and CM−CM interactions for single-cell hiPSC-CMs. We hypothesized that utilizing dual-protein patterning to imitate CM-ECM and CM−CM interactions would improve hiPSC-CM structure, *e.g.*, cell spread area, sarcomere alignment, and contractile function, *i.e.*, sarcomere contractility and total force production.

RESULTS AND DISCUSSION

Fabrication of Single- and Dual-Protein Patterned Polyacrylamide Hydrogels. To imitate both CM-ECM and CM−CM interactions, we developed a method for spatially accurate patterning of two proteins using Primo (Alvéole), a commercially available light-induced molecular adsorption patterning (LIMAP) tool.

A thorough description of the protocol can be found in the "Protein patterning glass coverslips" section within Methods and an overview of the protocol can be seen in Figure 1a. Briefly, we plasma treated a glass coverslip and incubated it with a blocking molecule, poly(L-lysine)-*graft*-poly(ethylene glycol) (PLL-*g*-PEG). We then added the proprietary photoinitiator, PLPP (Alvéole), and created our first pattern, the end caps, with UV exposure via Primo. We then incubated our first protein, in this case Protein A, a linking protein that is necessary to orient N-cadherin correctly for cell attachment.[30,31] After Protein A incubation, we added PLPP again and created our second pattern, the body, as well as our single-protein patterns using Primo. We incubated with our second protein, laminin, and began making our polyacrylamide hydrogels. We made polyacrylamide precursor solutions with oxidized *N*-Hydroxyethyl acrylamide (oHEA) to create covalent bonds between the protein patterns and the hydrogels. After beginning polymerization, we pipetted the solution onto a silanized glass coverslip and placed the protein-patterned glass coverslip on top of the solution (Figure 1b). After the hydrogel fully polymerized, we removed the top coverslip and incubated with N-cadherin. A schematic of the final result, a functionalized polyacrylamide hydrogel with single- and dual-protein patterns is shown in Figure 1c.

We created an array of single-cell patterns alternating between the two pattern types: (i) single-protein patterns consisting of laminin rectangles, and (ii) dual-protein patterns, consisting of laminin rectangles flanked by N-cadherin caps (Figure 1d). We verified the patterning and pattern transfer to PA hydrogel using a laminin antibody and a pan-cadherin antibody (Figure 1d). Finally, we seeded hiPSC-CMs on the patterns (Figure 1e) and assessed their morphology, force production, and sarcomere organization and contractility on the laminin-only and dual-protein patterns.

Our method provides a unique approach to multiprotein patterning that allows for accurate patterns and is compatible with a wide variety of device fabrication protocols.

Previous studies have created multiprotein patterns using Primo and other similar photopatterning tools, but each had constraints that limited our ability to use them. One study used Primo to create crossing line patterns with laminin and fibronectin.[32] In this study, the authors used a glass-bottom 6-well plate to ensure the orientation of the patterns did not change between patterning steps. To align the two protein patterns, they used PDMS stencils to create smaller wells within each well of the plate and then aligned the smaller well boundary with the digital ROI in the Primo software.[32] This method does not allow for micron-level accuracy in pattern alignment, limiting the use of the method in studies with more complex patterns. Additionally, patterning on a 6-well plate prevents the transfer of protein patterns to a hydrogel. Another study used a custom LIMAP setup to create intricate multiprotein patterns.[33] In this study, the substrate was not moved from the LIMAP system between patterning steps and of the various proteins used in patterning, the longest incubation was 15 min.[33] This limits the proteins that can be patterned and the applications that can be used with this method, as many proteins require incubation of at least an hour and many proteins must also be incubated in refrigerated conditions.

Mechanical Characterization of Polyacrylamide Hydrogels. We sought to mimic the elastic modulus of healthy human myocardium (5−10 kPa)[4,34] with our functionalized polyacrylamide hydrogels, as previous work has shown that substrate stiffness affects contractility in healthy and diseased hiPSC-CMs.[15,35] We indented multiple locations on multiple polyacrylamide hydrogels using an atomic force microscope (AFM) to characterize mechanical properties (Figure 2).

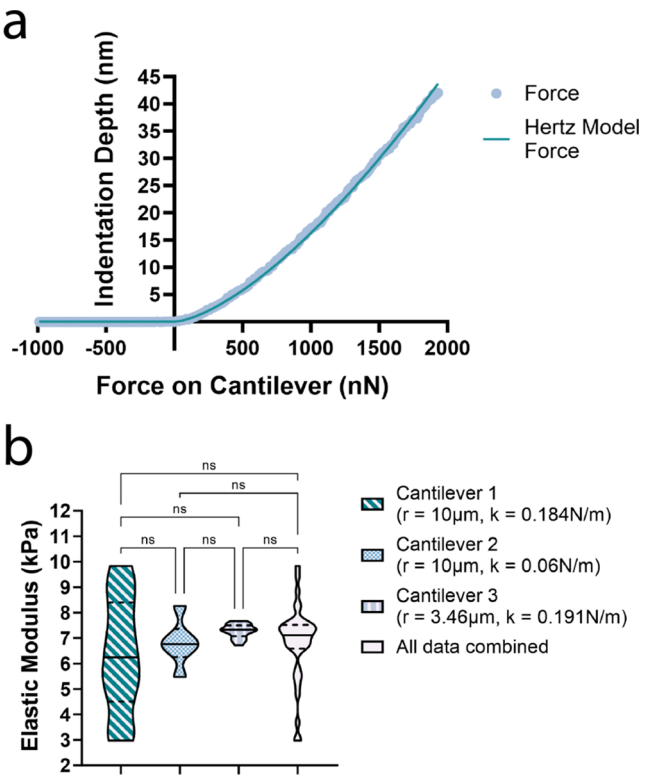

Figure 2. Mechanical characterization of polyacrylamide hydrogels. (a) Representative example of a force−indentation curve for a ∼6.8 kPa hydrogel, with measured force (light blue circular markers) plotted alongside the Hertz model calculated force (teal line). (b) PA hydrogel modulus measurements with each cantilever (n = 31). In (b), centerline = median, dotted lines = 25th and 75th percentiles.

Using the Hertz model (Figure 2a), we estimated a mean elastic modulus of 6.8 kPa with a standard deviation of 1.5 kPa. We used multiple AFM cantilevers for the measurements because PA hydrogel builds up on cantilever tips after ∼10−20 measurements. To ensure that variation between cantilevers was not skewing our results, we tested whether the moduli estimates from each cantilever were different. We used a Kruskal−Wallis one-way analysis of variance test because these

https://doi.org/10.1021/acsami.4c11934
ACS Appl. Mater. Interfaces 2025, 17, 174−186

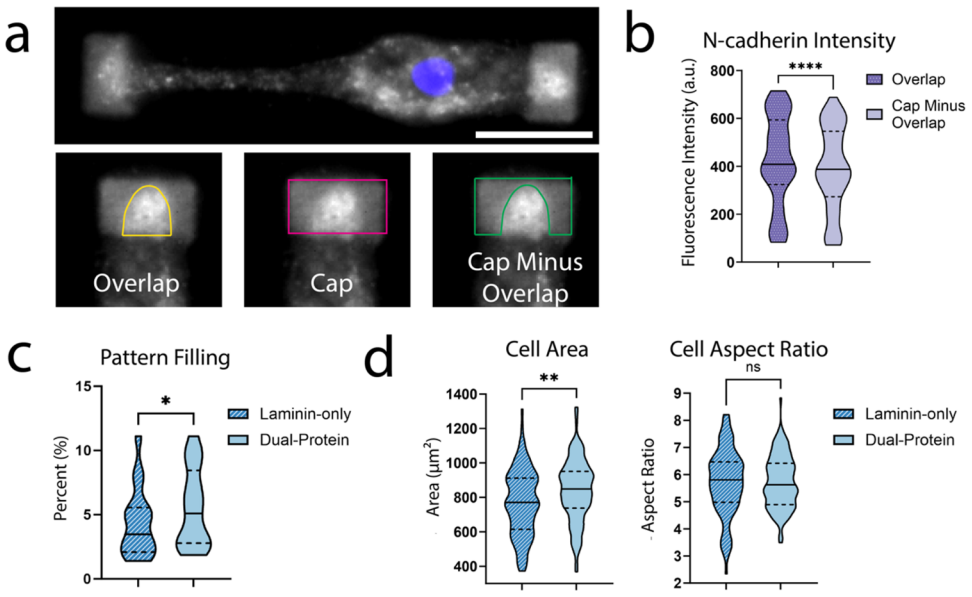

Figure 3. Dual-protein-patterned hiPSC-CMs have greater cell area than those on laminin-only patterns. (a) Verification of hiPSC-CM interaction with N-cadherin. hiPSC-CM stained for N-cadherin (gray) and cell nucleus (blue). Overlap of cell and N-cadherin measured using the outlines shown and (b) the resulting fluorescent intensities of the overlapping area and the end-cap area without the overlap are visualized in the plot to the right. For N-cadherin verification data, $n = 62$. (c) Pattern filling rates and (d) cell area and aspect ratio of hiPSC-CMs on laminin-only (right) and dual-protein (left) patterns. For pattern filling, cell area, and aspect ratio data, $n = 116$ for laminin-only patterned condition and $n = 131$ for dual-protein patterned condition. For all plots, centerlines indicate medians, dotted lines indicate 25th and 75th percentiles. *$p < 0.05$, **$p < 0.005$, ****$p < 0.0001$. Scale bar is 20 μm.

unpaired measurements were not normally distributed. We found no statistically significant difference between any of the data sets, including a data set containing all of the data points together (p-values between 0.44 and >0.9999; Figure 2b).

Validation of the hiPSC-CM Interaction with N-Cadherin on Dual-Protein Patterns. We first sought to verify that the hiPSC-CMs were interacting with the N-cadherin end caps on the dual-protein patterns. We stained hiPSC-CMs on dual-protein patterns with a pan-cadherin primary antibody and AlexaFluor-647 secondary antibody. We manually outlined each cell in FIJI (ImageJ) as described in Methods. We outlined the N-cadherin end-cap using the 647 nm channel (N-cadherin). We isolated the overlap between the cell outline and the N-cadherin end-cap and quantified the average fluorescence intensities in the overlap area and the N-cadherin end-cap area (Figure 3a).

We compared the area of cell-cap overlap to the cap area outside of the overlap using a two-tailed Wilcoxon matched-pairs signed rank test because neither data set was normally distributed, and each pair was compared within the same patterned cell. We observed a significant difference ($p < 0.0001$) between the intensity of N-cadherin signal where the hiPSC-CMs overlapped the N-cadherin patterns (422.4 ±186.9 au) and the intensity of the N-cadherin patterns themselves (387.4 ±174.2 au) (Figure 3b). This overlap confirms that the hiPSC-CMs localized endogenous N-cadherin on the *in vitro* N-cadherin patterns.

hiPSC-CMs on Dual-Protein Patterns Have Increased Cell Area and Attachment Rates. To investigate the effect of dual-protein patterns on hiPSC-CM structure, we assessed cell area and aspect ratio, as well as the rate of attachment of hiPSC-CMs to laminin-only and dual-protein patterns. Most studies that pattern hiPSC-CMs use rectangles with an aspect ratio of 5:1 to 7:1, corresponding to the range of adult human ventricular CMs.[1,15,16] In early experiments, we used patterns with an aspect ratio of 7:1, but found most cells did not fill the entire pattern, meaning many did not reach the N-cadherin end caps on the dual-protein patterns. We adjusted the length of the patterns to address this issue, bringing our pattern size and aspect ratio down to 14 μm × 85 μm and 6:1, respectively.

The cell area and aspect ratio of the hiPSC-CMs were assessed by drawing an outline of the cell in FIJI, as described in Methods. For the dual-protein patterned cells, we included only cells that overlapped at least one N-cadherin cap. The areas of hiPSC-CMs on dual-protein patterns were larger than those of laminin-only patterns, with average areas of 824.4 and 739.9 μm^2, respectively ($p = 0.0023$; Figure 3d). For reference, the total pattern area is 1190 μm^2. The discrepancy in cell and pattern area came from cells not reaching both end caps or not filling the entire width of the pattern, as can be seen in representative images in Supporting Information (Figure S1). The mean aspect ratios of hiPSC-CMs on the laminin-only and dual-protein patterns were 5.4 and 5.5 respectively (Figure 3d). The laminin-only patterned hiPSC-CMs had a larger variance than the dual-protein-patterned hiPSC-CMs, with standard deviations of 1.21 and 0.96, respectively (F-test $p = 0.0085$). The mean aspect ratios were compared using an unpaired, two-tailed t test with Welch's correction (this parametric test is used with data sets with unequal standard deviations) and had no significant difference ($p = 0.8705$). These results confirm that both laminin-only and dual-protein patterns support spreading of hiPSC-CM near the patterned aspect ratio.

In addition to hiPSC-CM area and aspect ratio, we considered whether the addition of N-cadherin end caps influenced the rate of cell attachment. To determine attachment rates, we counted the number of single-cell hiPSC-CMs attached to each pattern type and divided by the total number of patterns on the device. For this data, we included all cells on dual-protein patterns, regardless of whether they overlapped an N-cadherin end-cap or not. We

https://doi.org/10.1021/acsami.4c11934
ACS Appl. Mater. Interfaces 2025, 17, 174−186

assessed the difference in attachment rates using a parametric, two-tailed, ratio paired t test. The percentage of patterns filled was higher on dual-protein patterns than laminin-only patterns, with average pattern filling rates of 5.5 and 4.3% (of 216 and 144 dual- and single-protein patterns/device), respectively, on 17 total devices (p = 0.0441; Figure 3c). For the dual-protein pattern attachment data, we included all single hiPSC-CMs attached to patterns, even if they did not overlap either N-cadherin cap. For both data sets we included only single cells which had visible sarcomeres. While these pattern filling rates might appear low, it is not unusual for single-cell hiPSC-CM patterning. Frequently multiple hiPSC-CMs will attach to a single pattern, which then must be excluded. Additionally, fibroblasts or other cell types that are present in hiPSC-CM cultures[36] will bind to patterns, preventing hiPSC-CMs from attaching. The increased attachment rates on dual-protein patterns suggest that the N-cadherin patterns promote increased hiPSC-CM attachment, even if the hiPSC-CMs did not overlap the N-cadherin end caps at the time of fixation/imaging.

hiPSC-CMs on Dual-Protein Patterns Have Increased Contractility in the Direction of Sarcomere Alignment. To investigate the effect of dual-protein patterns on hiPSC-CM function, we analyzed the contractility of the hiPSC-CM sarcomeres from videos of beating CMs (Movies S1, S2, and S3). Sarcomeric contractility is a commonly used metric to compare hiPSC-CMs to adult human CMs, with adult human CMs exhibiting greater contractility than hiPSC-CMs.[1,4,15] We analyzed sarcomere contractility and organization using a previously published, open-source program called Sarc-Graph.[37] Sarc-Graph segments videos of fluorescently tagged sarcomeres in beating hiPSC-CMs and outputs parameters representing the orientation, spacing, and contractility of the sarcomeres, all of which are important metrics for hiPSC-CM structure and function.[37]

In overall sarcomere shortening, we did not see a significant difference between hiPSC-CMs on laminin-only vs dual-protein patterns (Figure 4a). The percent shortening is calculated by taking the difference between the maximum and minimum length for an individual sarcomere and dividing it by the average length of the sarcomere.[37] The percent sarcomere shortening for all of the sarcomeres in one cell are averaged to calculate a single percent sarcomere shortening for each hiPSC-CM. The mean percent sarcomere shortening for laminin-only and dual-protein patterns were not significantly different, with values of 16.89 and 17.67%, respectively (p = 0.6273).

To further investigate sarcomere contractility, we assessed $C_{||}$, a parameter calculated by Sarc-Graph that relates sarcomere contractility to sarcomere alignment and represents the shortening of the entire cell domain in the direction of dominant sarcomere orientation.[37] We found that hiPSC-CMs on dual-protein patterns had larger $C_{||}$ values, with an average of 0.041 compared to 0.029 for laminin-only patterned hiPSC-CMs (p = 0.0294; Figure 4a). This result suggests that the contractility of the sarcomeres along the long axis of the myofibrils is enhanced in hiPSC-CMs patterned with N-cadherin end caps mimicking CM−CM interactions. We determined the statistical significance with an unpaired t test with a Welch's correction for the unequal variance (F-test p = 0.0403) in the dual-protein-patterned data (standard deviation = 0.026) compared to the laminin-only patterned data (standard deviation = 0.019).

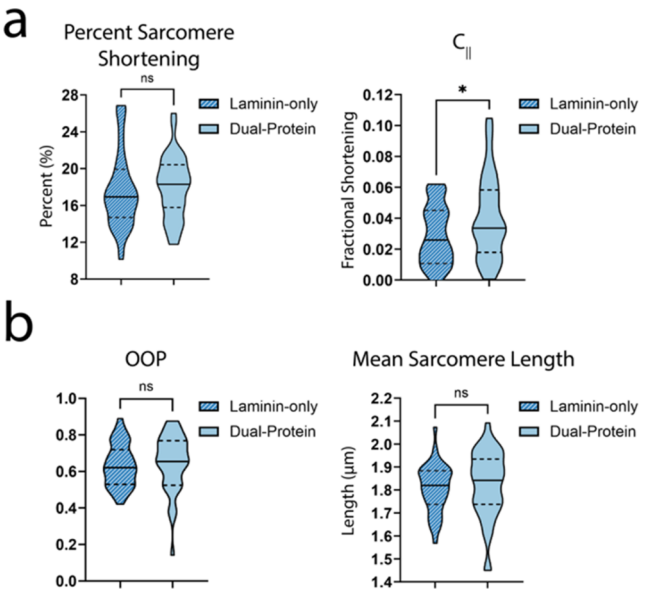

Figure 4. Dual-protein-patterned hiPSC-CMs have higher contractility in the direction of sarcomere organization, but no difference in sarcomere alignment compared to laminin-only patterned hiPSC-CMs. (a) Overall percent sarcomere shortening and fractional sarcomere shortening in the direction of sarcomere organization ($C_{||}$) for hiPSC-CMs on laminin-only and dual-protein patterns. (b) OOP and mean sarcomere length for hiPSC-CMs on laminin-only and dual-protein patterns. For both laminin-only and dual-protein patterned conditions, n = 39. For all plots, centerlines indicate medians, dotted lines indicate 25th and 75th percentiles. *p < 0.05.

hiPSC-CM Sarcomere Organization Is Similar on Laminin-Only and Dual-Protein Patterns. We further examined the impact of dual-protein patterning on hiPSC-CM structure by analyzing sarcomere structure and organization. Previous studies have suggested that adult CMs have average sarcomere lengths of ∼2.2 μm, while immature CMs have average sarcomere lengths of ∼1.6 μm[1]. To investigate sarcomere structure and organization, we assessed hiPSC-CM sarcomere lengths and the orientational order parameter (OOP), a metric commonly used to assess sarcomere organization in CMs that ranges from zero (random orientation) to 1 (perfectly aligned).[37] We hypothesized that hiPSC-CMs on dual-protein patterns would have more highly organized sarcomeres because previous studies found that N-cadherin is important in sarcomere formation and organization.[18,21−25]

However, sarcomeric organization, as assessed via the OOP, was not significantly different between hiPSC-CMs on laminin-only and dual-protein patterns, with average values of 0.6330 and 0.6254, respectively (p = 0.6205; Figure 4b). We also found no difference between the mean sarcomere lengths of hiPSC-CMs on laminin-only and dual-protein patterns. Both groups had mean sarcomere lengths of 1.8 μm, with minimum and maximum sarcomere lengths of 1.7 and 2 μm, respectively (p = 0.6193; Figure 4b). We assessed the statistical significance using an unpaired t test with a Welch's correction because the standard deviations of the laminin-only and dual-protein data, 0.10 and 0.14 μm, respectively, were significantly different (F-test p = 0.0408). These results suggest that the patterned N-cadherin end caps do not significantly increase organization beyond the organization improvements already achieved via matrix protein patterning.

https://doi.org/10.1021/acsami.4c11934
ACS Appl. Mater. Interfaces 2025, 17, 174−186

hiPSC-CM Force Production Is Similar on Laminin-Only and Dual-Protein Patterns. To further investigate the impact of dual-protein patterning on hiPSC-CM function, we assessed force production of hiPSC-CMs with Traction Force Microscopy (TFM), using the streamlined TFM module of a custom, open-source code called CONTRAX.[35] The streamlined TFM module of CONTRAX provides a user-friendly TFM analysis tool that reads in fluorescent microbead displacement videos and assesses a number of functional metrics, including traction force.[35,38] Example microbead displacement videos can be seen in Movies S2, S4, and S5. We looked at multiple parameters output by CONTRAX, including total force production, peak traction stress, average contraction displacement, and contraction velocity. We also assessed total contractile moment, which is a scalar value representing the sum of moments taken at the center of the cell,[39] and total impulse, which is the integrated area under the curve from the force versus time plot.[35] Force production, average contraction displacement, and contraction velocity are all directly related to hiPSC-CM contractility and are commonly used to assess CM function.[15,40,41] The peak traction stress avoids the homogenization caused by integrating over the cell area, providing insight into the maximum stress produced by each cell. The total contractile moment provides information about the distribution of stresses by weighting the traction forces by their distance from the cell center.[39]

We hypothesized that the force production of hiPSC-CMs might be more concentrated at the N-cadherin end caps compared to the hiPSC-CMs on laminin-only patterns. The total impulse is calculated by calculating the area under the force versus time trace.[35,42] Total impulse is thus equivalent to the tension-integral parameter used in a previous study that found that hypertrophic and dilated cardiomyopathies could be distinguished in murine CMs by their tension-integral magnitude.[42] We did not expect to see a difference in total impulse between our two conditions both using "healthy" hiPSC-CMs, but we assessed the parameter to learn if our conditions elicited a difference. For all of these parameters except for average contraction displacement and contraction velocity, we used the peak measurements, meaning the values calculated when the cell is either fully contracted or fully relaxed. Our analysis tools assume these are quasi-static states; however, we note this assumption is violated during active contraction or relaxation occurring across all frames of our ~800 frame videos.

We did not find significant differences between total force, peak stress, average contraction displacement, contraction velocity, total contractile moment, or total impulse (Figure 5). These results are consistent with the overall contractility results, suggesting that the difference in functional outputs of hiPSC-CMs on laminin-only and dual-protein patterns are modest. Within both laminin-only and dual-protein pattern conditions, we saw a large variance in force production, as can be seen in Figure 5a. For the laminin-only patterned hiPSC-CMs, the mean force was 104.1 ± 98.2 nN, while the dual-protein-patterned hiPSC-CMs had an average force of 118.3 ± 107.1 nN.

All of the parameters reported by CONTRAX, including those assessed above, are single scalar values for each cell. These parameters allow for quantification of force production but result in the loss of spatial information on hiPSC-CM contractility. This flattening of spatially distributed forces into scalar values is necessary to quantify and assess data sets that

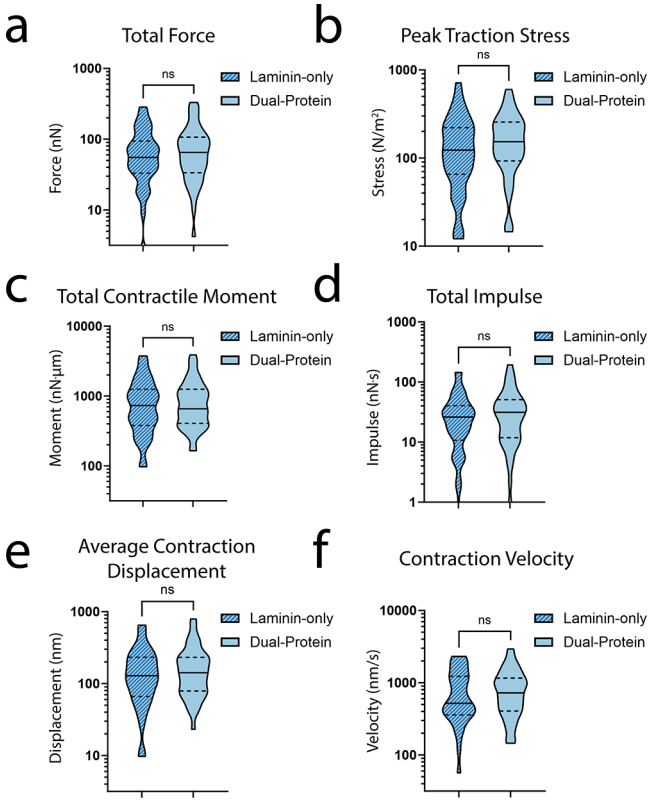

Figure 5. Dual-protein-patterned hiPSC-CMs demonstrate no difference in (a) total force, (b) peak traction stress, (c) total contractile moment, (d) total impulse, (e) average contraction displacement, and (f) contraction velocity compared to laminin-only patterned hiPSC-CMs. For all data in this figure, $N = 79$ with $n = 35$ for laminin-only and $n = 44$ for dual-protein condition. For all plots, centerline = median, dotted lines = 25th and 75th percentiles.

consist of ~800 frames per video and hundreds of displacement data points in each frame of each video. While the scalar outputs provide quantifiable comparisons between cells, the spatial data can contain differences in force distribution that are not discernible in scalar variables. To investigate the spatial distribution of force production for each condition, we averaged the peak contraction traction stress heatmaps of all the cells in each condition (Figure 6), with 35 cells in the laminin-only condition and 44 cells in the dual-protein condition.

We observed that the peak stresses appear closer to the pattern centroid in dual-protein-patterned hiPSC-CMs compared to laminin-only patterned hiPSC-CMs. The inward shift in peak traction stress location for the hiPSC-CMs on dual-protein patterns could be reflecting the inward shift of the laminin pattern boundary compared to the laminin-only patterns. The red squares in Figure 6a indicate the location of the N-cadherin end caps and the peak traction stresses occur within the laminin portion of the dual-protein patterns. This suggests that primarily focal adhesions drive the traction force production in hiPSC-CMs on dual-protein patterns. Further, N-cadherin is not sufficient to elicit the force production increases observed in primary rat and murine CM pairs. This lack of force production over the N-cadherin patterns by hiPSC-CM suggests that other features of the intercalated disc, such as desmosomes or signaling via gap junctions, or

https://doi.org/10.1021/acsami.4c11934
ACS Appl. Mater. Interfaces 2025, 17, 174−186

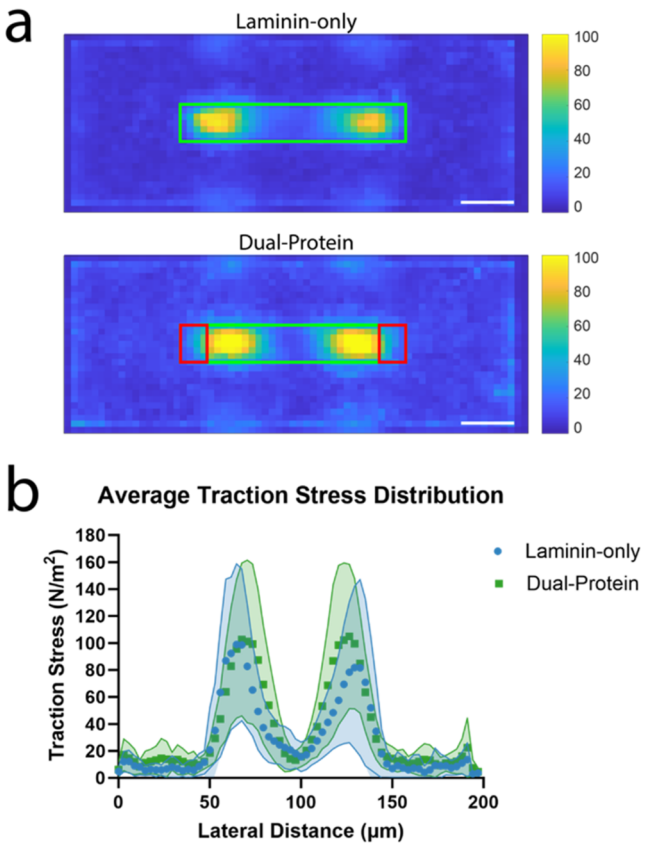

Figure 6. Spatial distribution of average traction stresses produced by hiPSC-CMs on laminin-only and dual-protein patterns. (a) Peak contraction traction stress heatmaps averaged over all cells in both laminin-only (n = 35) and dual-protein (n = 44) conditions. Green rectangles represent an estimation of the locations of laminin patterns, red rectangles represent an estimation of the locations of N-cadherin patterns. Color bars are in units of pascals. (b) Mean traction stress distribution with respect to lateral distance, averaged over a ∼10 μm width in the center of each heatmap. The shaded areas represent the standard deviations. Scale bars are 20 μm.

mechanical feedback via the partner cell,[19,43] may be necessary to drive increased contractility hiPSC-CM.

While the location of peak traction stress appears to have moved toward the cell center, the area of the peak traction stress is larger in dual-protein-patterned hiPSC-CMs compared to laminin-only patterned hiPSC-CMs. The areas of peak traction stress for the laminin-only patterns have a mean area of 162 μm^2. For the dual-protein patterns, the areas of peak traction stress have an mean area of 301 μm^2. While peak contractile tractions localize near the edges of the laminin pattern in both cases, the improvements in sarcomere coordination on hiPSC-CMs on dual-protein patterns suggest that N-cadherin-mediated mechanotransduction drives increased areas of mechanical connection to the patterns.

CONCLUSIONS

In this work, we have developed a method to observe the dynamics of hiPSC-CM on multiple proteins precisely patterned on a deformable hydrogel devices for TFM. We developed a method to pattern covalently linked laminin and N-cadherin on polyacrylamide hydrogels and applied this method to create patterns mimicking cell−cell and cell-ECM interactions for hiPSC-CMs. Our method provides the potential for more complex protein patterning of live cells for mechanobiological studies, expanding the possibilities for in vitro studies of various single-cell model systems. We applied our dual-protein patterning method to hiPSC-CMs and investigated the effect of dual-protein patterning on the dynamics of hiPSC-CMs, their sarcomeres and contractile forces. We found that our dual-protein patterning increased hiPSC-CM attachment rates, spread area, and the efficiency of sarcomere contraction along myofibrils. We observed no significant difference in force production, overall sarcomere contractility, and sarcomere organization between laminin-only and dual-protein patterned hiPSC-CMs, suggesting that N-cadherin end caps offer modest organizational improvements over patterning only matrix proteins.

This study was motivated by previous work that has demonstrated that connecting stem cell-derived CMs in pairs and lines increases contractility and sarcomeric organization and structure compared to single stem cell-derived CMs.[44,45] We wanted to see how much of this improvement could be recapitulated by patterning single hiPSC-CMs on the traditional ECM patterns with N-cadherin added to ends to replicate CM−CM junctions. We found that not only did it not improve contractile force, it actually pushed the force production away from the edge of the pattern (Figure 6).

We have identified multiple future directions that could be pursued with the method we developed here to recapitulate the improvement in contractility seen in hiPSC-CM pairs or lines. One potential direction is to investigate various ECM proteins used in the single- and dual-protein patterns. There are a wide range of ECM proteins that CMs interact with and these could affect the contractility of the hiPSC-CMs. Additionally, further examination of protein concentrations and the ratio between the density of body and end-cap proteins available for the hiPSC-CMs to attach to could provide useful insights into hiPSC-CM adhesion on these patterns. In addition to the protein density on the substrate surface, it would be useful to probe the intracellular N-cadherin signal to identify the degree of interaction between the hiPSC-CMs and the N-cadherin patterns. In preliminary experiments, we determined that we can adhere hiPSC-CMs to rectangular N-cadherin patterns on PA hydrogels using a covalent linker (oHEA) (Figure S2e). This confirms that N-cadherin can facilitate adhesion to a PA hydrogel but it does not confirm the creation of a fully functional adherens junction or linkage between the N-cadherin adhesion and the cytoskeleton. In future work, super-resolution imaging methods could be employed to investigate the intracellular response to N-cadherin attachment on PA hydrogels.

Beyond further characterization of N-cadherin and ECM protein patterns, we have considered that additional coordination, beyond N-cadherin signaling, could be necessary to increase force production in hiPSC-CM pairs and lines. Other proteins present in CM−CM junctions, such as desmoglein, desmocollin, or connexin43, could be used individually or in a cocktail with N-cadherin for the end-cap patterns to determine if these other proteins are key to the increased contractility seen in hiPSC-CM pairs. Alternatively, the additional mechanical loading on an hiPSC-CM due to neighboring hiPSC-CM contraction could drive increased contractility, rather than CM−CM junction signaling. This could be investigated by stretching patterned hiPSC-CMs to identify if additional mechanical loading is correlated with higher contractile force.

https://doi.org/10.1021/acsami.4c11934
ACS Appl. Mater. Interfaces 2025, 17, 174−186

Despite the lack of hiPSC-CM contractility improvement, this method provides a new approach to creating multiprotein patterns. This method is well suited for testing different pattern geometries as well as different proteins. It also can be used with any imaging-based tests, such as calcium signaling or patch-clamp assays, making it a versatile tool for mechanobiological studies.

METHODS

Protein Patterning Glass Coverslips. N-cadherin is an asymmetric protein and a linking protein is necessary to ensure the extracellular binding site is available when patterning N-cadherin.[29,30,46] In this work, we used an N-cadherin Fc chimera (R&D Systems, 1388-NC-050) and a 546 nm fluorescently tagged Protein A (ThermoFisher, P11049) as our linking protein. Protein A is a protein with a high affinity to Fc-regions of IgG molecules.[47] It has been previously used to ensure the correct orientation of E-cadherin.[30,31] The Fc region of the N-cadherin chimera protein binds to the Protein A, ensuring the correct orientation of the N-cadherin on the device surface.

To begin protein micropatterning, we activated 18 mm diameter #1 glass coverslips with oxygen plasma for 5 min at 18 W (Harrick, PDC-32G). Immediately after plasma treatment, we sealed an 8 mm inner diameter silicone ring (B&J Rubber Products) to the center of the glass coverslip. The silicone ring was cut from a Silhouette CAMEO 3 electronic desktop cutter (Silhouette America). We immediately pipetted a solution of 100 μg/mL of poly(L-lysine)-*graft*-poly-(ethylene glycol) (PLL(20)-g[3.5]- PEG(2); SuSoS AG) diluted in phosphate buffered saline (PBS; Gibco, ThermoFisher, 10010049) within the ring and incubated for 1 h at room temperature. We rinsed the PLL-*g*-PEG thoroughly (10×) with PBS prior to micropatterning. Following PLL-*g*-PEG incubation and rinsing, we pipetted 20 μL of UV sensitive photoinitiator (PLPP; Alvéole) into the silicone ring on the glass coverslip. Then we placed the glass coverslip on the stage of a Leico Dmi8 epifluorescence microscope equipped with a Fluotar 20*x*/0.40 NA objective and the Alvéole Primo photopatterning system (Alvéole) with a 375 nm, 7.10 mW laser. We made digital masks for the Protein A "end-cap" patterns as well as the main laminin patterns using the open-source software Inkscape (https://inkscape.org). We used the pixel-to-micron ratio generated by Primo calibration to define the geometries of all patterns. We defined two patterns for constraining the single-cell hiPSC-CM: (1) 14 μm × 85 μm laminin-only patterns and (2) 14 μm × 85 μm dual-protein patterns. Dual-protein patterns are comprised of Protein A end-cap patterns (14 μm × 10 μm) overlapped with laminin rectangles (14 μm × 69 μm) by ∼10% to mitigate any alignment artifacts.

We loaded the digital masks into the Leonardo plugin (Alvéole Laboratory) on Micro-Manager software,[48] and made a 6 by 6 array with 150 μm spacing between each instance of the patterns. We illuminated the glass coverslip with the first digital mask for the Protein A end caps at a dosage of 1,000 mJ/mm^2. Following micropatterning, we rinsed off the photoinitiator with PBS and incubated the glass coverslip with 100 μL of a 100-μg/mL solution of 546 nm fluorescently tagged Protein A overnight at 4 °C. We then thoroughly rinsed the Protein A from the glass coverslip using PBS and added another 20 μL of PLPP photoinitiator. We illuminated the glass coverslip with the second digital mask for the laminin rectangles at a dosage of 1000 mJ/mm^2. We designed the array of patterns to alternate between dual-protein and laminin-only patterns. Before UV illumination, we aligned the shortened laminin bodies within the digital mask to the already-patterned Protein A end-cap patterns using a Texas Red fluorescent excitation filter. Following this second UV illumination step, we rinsed off the photoinitiator with PBS and incubated the glass coverslip with a 500-μg/mL solution of laminin (Corning, 354232) for 2 h at room temperature. For pattern verification experiments, we incubated the glass coverslip with a 500-μg/mL solution of green fluorescent laminin (Cytoskeleton, Inc., LMN02) for 2 h at room temperature. This laminin product is derived from mouse tumors, which were previously reported to be rich in laminin 111;[49] laminin 111 isoform is thought to be important in normal cardiac development.[50] Finally, we rinsed the patterns with PBS and removed the silicone containment ring prior to gel transfer. A schematic of the protein micropatterning process flow can be seen in Figure 1a.

Preparation of Polyacrylamide (PA) Hydrogels. In preliminary work, the Protein A::N-cadherin complex could not anchor hiPSC-CMs on unfunctionalized polyacrylamide (PA) hydrogels (Figures S2−S5), so we employed oxidized *N*-Hydroxyethyl acrylamide (oHEA) to create a covalent bond between the hydrogel and the Protein A. We transferred the laminin and Protein A patterns to oHEA-functionalized PA hydrogel before adding N-cadherin, to ensure that the final hydrogel presented the N-cadherin binding domain on the hydrogel surface.

We prepared the oHEA-functionalized PA hydrogels following a previously published protocol with some modifications.[12,51] Briefly, we began by oxidizing *N*-Hydroxyethyl acrylamide (HEA; Sigma, 697931) by adding 0.01 g of sodium metaperiodate (Sigma, 71859) to 2.338 mL of HEA, then incubating in the dark on a shaker for 4 h. To adhere the PA hydrogels to the glass-bottom dishes used in this work, we treated the glass with bind-silane. We prepared a solution with 95 μL of 100% ethanol, 50 μL of acetic acid, and 3 μL of 3-(Trimethoxysilyl)propyl methacrylate (Bind-silane; Sigma, M6514). Then, we treated the glass with oxygen plasma for 30 s at 18 W (Harrick, PDC-32G). Directly after plasma treating the glass, we added ∼50 μL of the bind-silane solution to the glass surface. We incubated the solution on the glass for 1 min, after which we removed the excess bind-silane solution. We left the remaining solution to react for 10 min, after which we rinsed the glass twice with 1 mL of 100% ethanol and dried with nitrogen gas.

To prepare the PA hydrogel solution, we combined 732 μL of 40% Acrylamide solution (Bio-Rad, 1610140) and 260 μL of 2% Bis-acrylamide solution (Bio-Rad, 1610142) with 4.008 mL Milli-Q water. For experiments used in TFM analysis, we added 326 μL of 1.0-μm diameter blue fluorescent microbeads (ThermoFisher, F8814) and decreased the Milli-Q volume to 3.682 mL to maintain the total volume of 5 mL. Finally, we added 200 μL of oxidized HEA, bringing the total volume to 5.2 mL. Separately, we prepared a 10% weight by volume (w/v) solution of ammonium persulfate (APS; Sigma, A9164) in Milli-Q water.

To begin polymerization, we added 2.6 μL of *N*,*N*,*N*′,*N*′-tetramethylethylenediamine (TEMED; Sigma, 411019) and 260 μL of the 10% w/v APS solution to the PA solution. We gently mixed the solution with a P1000 pipet and then pipetted 35 μL of the solution onto the bind-silane-treated glass surface. We then placed a protein patterned coverslip on top of the solution, sandwiching the PA solution between the bind-silane-treated glass and the protein patterned glass. After casting, the hydrogel polymerized in the dark for 30 min before we hydrated it with PBS and left it to fully polymerize at 4 °C for 6−8 h. After full polymerization, we removed and discarded the protein patterned top coverslip. A schematic of the protein transfer to oHEA-functionalized PA hydrogel can be seen in Figure 1b.

Following the removal of the top coverslip, we aspirated the PBS from the dish and incubated each PA hydrogel with ∼50 μL of 100-μg/mL N-cadherin (R&D Systems, 1388-NC-050) for 3 h at 4°C. After 3 h, we washed the PA hydrogel three times with 1 mL PBS and then stored it overnight at 4 °C in PBS with 10% Antibiotic-Antimycotic 100× (Anti-Anti; Gibco, ThermoFisher, 15-240-062) and 1% bovine serum albumin (BSA; ThermoFisher, PI37525). The following day, we washed the hydrogel three times with 1 mL PBS and then stored it in PBS + 10% Anti-Anti until cell seeding. A schematic of the final device can be seen in Figure 1c.

We verified the patterning and the pattern transfer to PA hydrogel using green fluorescent laminin (as described in *Protein patterning glass coverslips*) and a pan-cadherin primary antibody (Sigma, C3678). We diluted the pan-cadherin antibody 1:200 in PBS and incubated on the devices for 1 h at room temperature. We washed the devices three times with PBS and then incubated the devices with antirabbit AF-647

https://doi.org/10.1021/acsami.4c11934
ACS Appl. Mater. Interfaces 2025, 17, 174−186

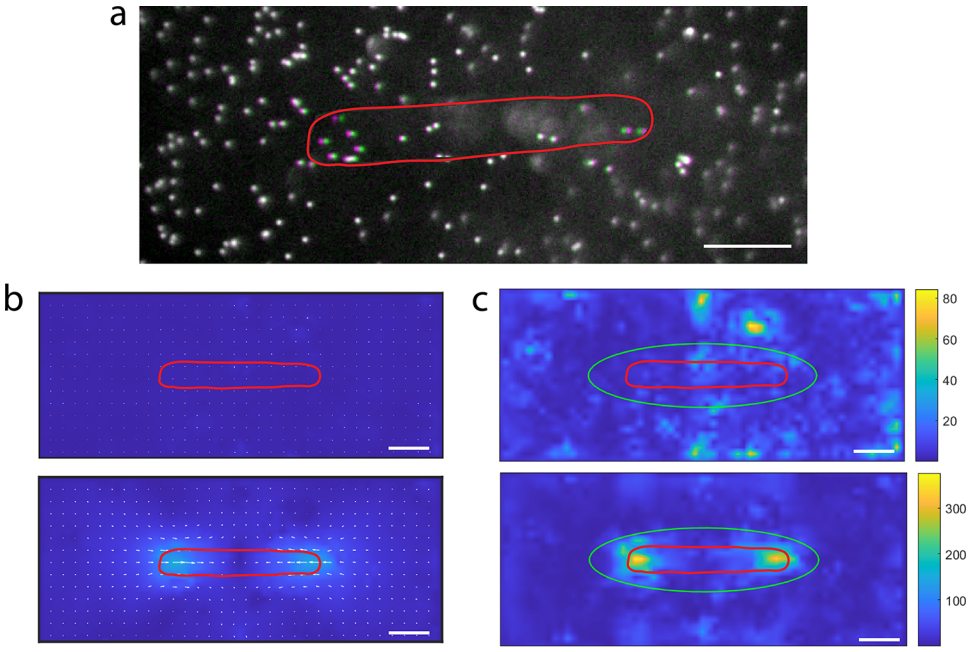

Figure 7. Intermediate steps of traction force microscopy. (a) Representative image of fluorescent microbeads when cell is fully relaxed (magenta) and fully contracted (green) state. Representative images of (b) displacement maps and (c) traction stress maps at relaxed (top) and contracted (bottom) states. Color bars in (c) are in units of pascals. In all images, red elliptical shape is cell outline. In (c), green ellipse is the analysis region used by CONTRAX. Scale bars are 20 μm. For representative examples of full bead videos, displacement map videos, and traction stress map videos, see Supporting Information.

diluted 1:500 in PBS for 1 h at room temperature. We rinsed the devices three times with PBS and then imaged (Figure 1d).

Mechanical Characterization by Atomic Force Microscopy (AFM). We used AFM indentation to estimate the elastic modulus of our hydrogels, based on a previously published protocol.[52] Briefly, we used a WITec AFM (Alpha300) and large tip cantilevers with the following tip radii of curvature (r_t) and nominal spring constants (k_c): (1) r_t = 10 μm, k_c = 0.184 N/m, sensitivity = 0.047 V/nm (Bruker, SAA-SPH-10UM), (2) r_t = 10 μm, k_c = 0.060 N/m, sensitivity = 0.027 V/nm (MLCT-SPH-10UM), and (3) r_t = 3.46 μm, k_c = 0.191 N/m, sensitivity = 0.042 V/nm (Bruker, SAA-HPI). We measured four hydrogels, assessing 3 locations per hydrogel with 2−3 measurements per location. Each hydrogel was measured 2 days after polymerization.

The PA hydrogels were attached to a glass-bottom dish and submerged in PBS. We measured Optical Lever Sensitivities[53] before each experiment by performing force−distance scans against the glass surface of a glass-bottom plate using the following parameters: feedback control with 1.0 V set point, 1% p-gain, and 0.2% i-gain, force−distance using 0.2 μm pull and 0.6 μm push at 0.2 μm/s speed.

After determining the Optical Lever Sensitivity, we loaded the PA hydrogel sample and centered the cantilever above a point on the hydrogel. We then approached the surface using the following parameters: 1.0 V set point, 1% p-gain, and 0.2% i-gain. We then performed the force−distance curve measurement using WITec's Distance Curve mode with approach and retract distances of 20 and 10 μm, respectively, at a speed of 3 μm/s. We analyzed the force−distance curves using the Hertz model,[54] with the assumption that the PA hydrogel is linearly elastic.

Stem Cell Culture and Cardiomyocyte Differentiation. For this work, we used human induced pluripotent stem cell-derived cardiomyocytes (hiPSC-CMs). The hiPSCs were GFP-tagged α-actinin-2 (cell line 75) developed at the Allen Institute for Cell Science (allencell.org/cell-catalog) and available through Coriell (AICS-0075-085).[55,56] We cultured the hiPSCs on tissue culture plastic coated in Matrigel (Corning, 356252) using feeder-free culture conditions in standard conditions of 5% carbon dioxide at 37 °C. The hiPSCs were cultured in Essential 8 Medium (Gibco, ThermoFisher, A1517001) which was changed daily. We passaged the cells with EDTA when confluency reached 75%. We differentiated the hiPSCs into cardiomyocytes (hiPSC-CMs) using a previously published protocol[57] and maintained the hiPSC-CMs until seeding in RPMI 1640 Medium (ThermoFisher, 11875119) with B-27 Supplement (B27; ThermoFisher, 17504044). We seeded the hiPSC-CMs on devices at a density of ∼100,000 cells/cm^2 between day 24−30 and imaged 3−4 days after seeding (day 27−34).

Microscopy. We performed all microscopy with a Zeiss Axio Observer 7 inverted microscope with a high speed camera (Photometrics Prime 95b) and a water immersion 40× objective (Plan Apochromat, 1.2 NA). The microscope was equipped with an incubation chamber (PeCon) that maintained a temperature of 37 °C and 5% CO_2 during live-cell imaging.

Before live-cell imaging, we changed the media from B27 to B-27 Supplement in RPMI 1640 Medium, no phenol red (ThermoFisher, 11835030) with 10-mM HEPES and 1% Anti-Anti. While imaging, we electrically paced the hiPSC-CMs with pulses of electric-field stimulation at 10−15 V with a frequency of 1 Hz (Myopacer, IonOptix). For each cell, we took a still image in brightfield, 405 (fluorescent microbeads), 488 (α-actinin), and 546 (Protein A). We used the still images in the 546 channel to determine whether the cell was on a laminin-only or dual-protein pattern. After the still images, we recorded ∼10 s long videos of sarcomeres (488 channel) and fluorescent microbeads (405 channel). The frame rate was ∼40 frames per second for the sarcomere videos and ∼80 frames per second for the microbeads videos.

For the data presented in this work, unless otherwise noted, we included only cells that overlapped at least one N-cadherin end-cap in the dual-protein data sets. For traction force microscopy data, we included only cells with a beating frequency above 0.4 Hz and below 1.6 Hz.

Sarcomere Contractility Quantification. We acquired sarcomere shortening videos using α-actinin::GFP-tagged hiPSC-CMs (as described in *Stem cell culture and cardiomyocyte differentiation*). After collecting a video, we cropped it in FIJI (ImageJ)[58] and applied the "Subtract Background" tool with a rolling ball radius of 5 pixels. We then adjusted the brightness and contrast in FIJI using the "auto"

https://doi.org/10.1021/acsami.4c11934
ACS Appl. Mater. Interfaces 2025, 17, 174−186

option and saved the video as an AVI with a 40 frames per second frame rate.

To quantify the average alignment, sarcomere length, sarcomere shortening, and radial contraction, we used Sarc-Graph, a previously published, open-source code that segments the images in each video and tracks sarcomere alignment and contraction.[37]

Sarc-Graph assesses the average alignment using the orientational order parameter (OOP), a metric commonly used to assess sarcomere organization in CMs that ranges from zero (random orientation) to 1 (perfectly aligned).[37] Sarcomere shortening is calculated in Sarc-Graph by dividing the difference between the maximum and minimum length for an individual sarcomere by the average length of the sarcomere. Sarcomere shortening for all of the sarcomeres in one cell are averaged to calculate a single percent sarcomere shortening for each hiPSC-CM.[37] Radial contraction is assessed in Sarc-Graph using the parameter $C_{||}$, a more complex parameter that is calculated using continuum mechanics and represents the fractional shortening of the sarcomeres in the direction of sarcomere alignment. For a detailed description of how $C_{||}$ is calculated, see Zhao et al.[37]

Traction Force Microscopy. We utilized CONTRAX, a custom, open-source workflow that acquires images and videos, then analyses fluorescent bead displacements using an Ncorr tracking module on pairwise frames from videos of beating hiPSC-CMs to generate matrices of spatiotemporal displacement field data.[35] The traction force microscopy (TFM) module in CONTRAX uses the displacements to calculate traction stresses. The traction stresses are then integrated over the area of the cell to determine the total traction force produced by the cell.[35]

We first uploaded bead displacement videos (~800 frames each) and their corresponding brightfield still images into CONTRAX. For each video, we drew the outline of the cell in FIJI using a composite image of the brightfield and 488 still images of the cell. We saved the cell outline as an ROI and loaded it into CONTRAX with the corresponding bead displacement video (Figure 7a). CONTRAX uses the cell outline to isolate the forces produced by the cell from background noise. The size of the area around the cell included in the analysis can be set using the "mask parameters" in CONTRAX.

Force production is calculated from bead displacements, so we can expect to see forces slightly outside of the cell outline due to the cell deforming the gel at the cell boundary, causing bead displacements outside the cell outline, as can be seen in Figure 7a. To capture the forces at the cell boundary, while excluding background noise, we adjusted the "area factor" and "scale factor" in the "mask parameters" section of CONTRAX. After outlining the cell, CONTRAX calculates an ellipse that best fits the outline. The area included in the analysis is equal to the best fit ellipse times the "area factor", so a larger "area factor" equals a larger analyzed area. The "scale factor" controls the aspect ratio of the analysis region ellipse, with a "scale factor" of greater than 1 increasing the aspect ratio and a "scale factor" of less than 1 decreasing the aspect ratio.

In this work, we chose an analysis region "area factor" of 3 and a "scale factor" of 0.75. The area factor of 3 allows us to capture the forces just outside the cell boundary as described above, while excluding much of the noise around the cell, as can be seen in Figure 7c. The "scale factor" of 0.75 ensures the analysis region stays within the frame, especially with long, thin cells.

After loading the cell outline, we input the material properties for the PA hydrogel the cell was on. For this study, all the cells were cultured on PA hydrogels with a Young's modulus of ~6.8 kPa. The Poisson's ratio for PA hydrogels is generally accepted to be between 0.45 and 0.5,[59−61] and in this work, we used a Poisson's ratio of 0.45. These parameters are used in the force calculation with the assumption that the gel is linearly elastic and homogeneous, which is a generally accepted approximation when the strain on the hydrogel is very small (less than 1), as it is in TFM.[60] Additionally, we assume that the gel is thick enough and wide enough to prevent the cells from experiencing any boundary effects of the gel and that all cell-produced forces normal to the hydrogel surface are negligible. These assumptions are approximately true given that the hydrogel is ~10 times as thick as the cell height[62] and are generally accepted assumptions for traction force microscopy.[17,60,62]

After the video initialization, we set the displacement parameters for the Ncorr displacement tracking module. We used a subset radius of 30 px, spacing coefficient of 10 px, cutoff norm of 1e-6, and cutoff iteration of 20. These parameters are used to optimize the bead tracking in Ncorr, minimizing the amplification of noise and the loss of information due to oversmoothing. Using the resulting displacement maps at each time point (Figure 7b), CONTRAX calculates the regularization parameter, lambda, based on L-curve optimization.[63] The regularization parameter constrains the accepted force vectors, minimizing the error due to noise and the error due oversmoothing. Finally, using this regularization parameter, CONTRAX calculates the traction force heatmaps for each time point (Figure 7c) using Fourier Transform Traction Cytometry (FTTC).[39,64]

Cell Fixation and Immunostaining. Following live-cell imaging, we fixed the hiPSC-CMs with 4% formaldehyde (ThermoFisher, 28908) for 10 min. Then we washed the cells with PBS three times and stored them in PBS at 4 °C until immunostaining. Before antibody incubation, we incubated the cells for 5 min with a permeabilization solution of 0.1% Triton X-100 (ThermoFisher, A16046.AE) in PBS. We then incubated them with a blocking solution of 0.3% Tween20 (ThermoFisher, 28352) and 2% BSA in PBS for 30 min. We diluted a pan-cadherin primary antibody (Sigma, C3678) 1:200 in a solution of 0.1% Tween20 and 1% BSA in PBS (dilution buffer). We incubated the hiPSC-CMs with the pan-cadherin antibody solution for 1 h at room temperature, then washed three times with dilution buffer. We diluted antirabbit AF-647 secondary antibody (ThermoFisher, A-32733) 1:500 in dilution buffer and incubated on the cells for 1 h at room temperature. We washed the cells three times with PBS and then stored in PBS at 4 °C until imaging.

Statistics. Unless otherwise noted, we determined statistical significance of the data presented using parametric, unpaired, two-tailed t tests. Significance p-values are indicated in all figures as follows: * = $p < 0.05$, ** = $p < 0.005$, *** = $p < 0.0005$, and **** = $p < 0.0001$. For all parametric t tests, we verified Normality and Lognormality and transformed data as appropriate. For all t tests, we also performed F-tests to check differences in variance between the two samples. Unless otherwise noted, all F-tests were not significant. For data with significant differences in variance, we reanalyzed the data with a Welch's correction to account for varying standard deviations. All statistical analyses were performed and visualized using Prism (GraphPad Software, Inc.).

■ ASSOCIATED CONTENT

Supporting Information

The Supporting Information is available free of charge at https://pubs.acs.org/doi/10.1021/acsami.4c11934.

Fluorescent images of hiPSC-CMs on single- and dual-protein patterns (Figure S1), brightfield images of hiPSC-CMs attached to Matrigel and N-cadherin patterns (Figure S2), fluorescent images of N-cadherin protein patterns before and after hiPSC-CM seeding (Figure S3), fluorescent images of N-cadherin protein patterns over time in hiPSC-CM media (Figure S4), fluorescent images of N-cadherin antibody controls experiments (Figure S5) (PDF)

Fluorescent video of hiPSC-CM sarcomeres beating—example 1 (Movie S1) (AVI)

Fluorescent video of microbeads embedded in PA hydrogel beneath a beating hiPSC-CM — example 1 (Movie S2) (AVI)

Fluorescent video of hiPSC-CM sarcomeres beating—example 2 (Movie S3) (AVI)

https://doi.org/10.1021/acsami.4c11934
ACS Appl. Mater. Interfaces 2025, 17, 174−186

Fluorescent video of microbeads embedded in PA hydrogel beneath a beating hiPSC-CM – example 2 (Movie S4) (AVI)

Fluorescent video of hiPSC-CM sarcomeres beating– example 3 (Movie S5) (AVI)

fluorescent video of microbeads embedded in PA hydrogel beneath a beating hiPSC-CM – example 3 (Movie S6) (AVI)

AUTHOR INFORMATION

Corresponding Author

Beth L. Pruitt – *Department of Mechanical Engineering, University of California, Santa Barbara, Santa Barbara, California 93106, United States; Biomolecular Science and Engineering Program and Department of Bioengineering, University of California, Santa Barbara, Santa Barbara, California 93106, United States;* orcid.org/0000-0002-4861-2124; Email: blp@ucsb.edu

Authors

Kerry V. Lane – *Department of Mechanical Engineering, University of California, Santa Barbara, Santa Barbara, California 93106, United States;* orcid.org/0000-0003-3099-9217

Liam P. Dow – *Biomolecular Science and Engineering Program, University of California, Santa Barbara, Santa Barbara, California 93106, United States*

Erica A. Castillo – *Department of Mechanical Engineering, University of California, Santa Barbara, Santa Barbara, California 93106, United States; Department of Mechanical Engineering, Stanford University, Stanford, California 94305, United States*

Rémi Boros – *Department of Physics, University of California, Santa Barbara, Santa Barbara, California 93106, United States*

Samuel D. Feinstein – *Department of Mechanical Engineering, University of California, Santa Barbara, Santa Barbara, California 93106, United States; Department of Bioengineering, University of California, Santa Barbara, Santa Barbara, California 93106, United States;* orcid.org/0009-0004-2374-5774

Gaspard Pardon – *AGORA Cancer Research Center, Swiss Federal Institute of Technology of Lausanne, Lausanne CH-1011, Switzerland*

Complete contact information is available at: https://pubs.acs.org/10.1021/acsami.4c11934

Author Contributions

[▽]K.V.L. and L.P.D. contributed equally to this work. K.V.L.: conceptualization, data curation, formal analysis, investigation, methodology, project administration, validation, visualization, and writing. L.P.D.: conceptualization, investigation, methodology, visualization, and writing. E.A.C.: conceptualization, methodology, and writing. R.B.: formal analysis and resources. S.D.F.: resources and writing. G.P.: conceptualization, software, and writing. B.L.P.: conceptualization, funding acquisition, resources, supervision, design of experiments, review and interpretation of data, and writing.

Notes

The authors declare no competing financial interest.

ACKNOWLEDGMENTS

This work was supported by National Institutes of Health grant 3RM1GM131981-02S1 and National Science Foundation CMMI-2227509 to B.L.P. K.V.L. was also supported by NSF GRFP (DGE-1650114) and UCSB fellowship funding, E.A.C. was also supported by NSF GFRP (DGE-1656518) and Ford Foundation Predoctoral Fellowship funding, and R.B. was supported by NSF-DMR-2004617. K.V.L. acknowledges useful conversations with Janae Gayle about the Sarc-Graph code. K.V.L. acknowledges support in hiPSC-CM culture from Trevor Pyle and Danny Gillissen. The authors acknowledge the use of the Nanostructures Cleanroom Facility within the California NanoSystems Institute, supported by the University of California, Santa Barbara and the University of California, Office of the President.

REFERENCES

(1) Yang, X.; Pabon, L.; Murry, C. E. Engineering adolescence: maturation of human pluripotent stem cell-derived cardiomyocytes. *Circ. Res.* **2014**, *114* (3), 511–523. From NLM Medline

(2) Chen, V. C.; Ye, J.; Shukla, P.; Hua, G.; Chen, D.; Lin, Z.; Liu, J. C.; Chai, J.; Gold, J.; Wu, J.; et al. Development of a scalable suspension culture for cardiac differentiation from human pluripotent stem cells. *Stem Cell Res.* **2015**, *15* (2), 365–375.

(3) Sayed, N.; Liu, C.; Wu, J. C. Translation of Human-Induced Pluripotent Stem Cells: From Clinical Trial in a Dish to Precision Medicine. *J. Am. Coll. Cardiol.* **2016**, *67* (18), 2161–2176.

(4) Schroer, A.; Pardon, G.; Castillo, E.; Blair, C.; Pruitt, B. Engineering hiPSC cardiomyocyte in vitro model systems for functional and structural assessment. *Prog. Biophys. Mol. Biol.* **2019**, *144*, 3–15.

(5) Zhang, J.; Wilson, G. F.; Soerens, A. G.; Koonce, C. H.; Yu, J.; Palecek, S. P.; Thomson, J. A.; Kamp, T. J. Functional cardiomyocytes derived from human induced pluripotent stem cells. *Circ. Res.* **2009**, *104* (4), e30–e41, DOI: 10.1161/CIRCRESAHA.108.192237.

(6) Ahmed, R. E.; Anzai, T.; Chanthra, N.; Uosaki, H. A Brief Review of Current Maturation Methods for Human Induced Pluripotent Stem Cells-Derived Cardiomyocytes. *Front. Cell Dev. Biol.* **2020**, *8*, 178.

(7) Sager, P. T.; Gintant, G.; Turner, J. R.; Pettit, S.; Stockbridge, N. Rechanneling the cardiac proarrhythmia safety paradigm: a meeting report from the Cardiac Safety Research Consortium. *Am. Heart J.* **2014**, *167* (3), 292–300.

(8) Crumb, W. J., Jr.; Vicente, J.; Johannesen, L.; Strauss, D. G. An evaluation of 30 clinical drugs against the comprehensive in vitro proarrhythmia assay (CiPA) proposed ion channel panel. *J. Pharmacol. Toxicol. Methods* **2016**, *81*, 251–262.

(9) Fermini, B.; Hancox, J. C.; Abi-Gerges, N.; Bridgland-Taylor, M.; Chaudhary, K. W.; Colatsky, T.; Correll, K.; Crumb, W.; Damiano, B.; Erdemli, G.; et al. A New Perspective in the Field of Cardiac Safety Testing through the Comprehensive In Vitro Proarrhythmia Assay Paradigm. *J. Biomol. Screening* **2016**, *21* (1), 1–11.

(10) Blair, C. A.; Pruitt, B. L. Mechanobiology Assays with Applications in Cardiomyocyte Biology and Cardiotoxicity. *Adv. Healthcare Mater.* **2020**, *9* (8), No. e1901656.

(11) Buikema, J. W.; Lee, S.; Goodyer, W. R.; Maas, R. G.; Chirikian, O.; Li, G.; Miao, Y.; Paige, S. L.; Lee, D.; Wu, H.; et al. Wnt Activation and Reduced Cell-Cell Contact Synergistically Induce Massive Expansion of Functional Human iPSC-Derived Cardiomyocytes. *Cell Stem Cell* **2020**, *27* (1), 50–63.e55.

(12) Sarker, B.; Walter, C.; Pathak, A. Direct Micropatterning of Extracellular Matrix Proteins on Functionalized Polyacrylamide Hydrogels Shows Geometric Regulation of Cell-Cell Junctions. *ACS Biomater. Sci. Eng.* **2018**, *4* (7), 2340–2349.

(13) Lee, S.; Yang, H.; Chen, C.; Venkatraman, S.; Darsha, A.; Wu, S. M.; Wu, J. C.; Seeger, T. Simple Lithography-Free Single Cell

Micropatterning using Laser-Cut Stencils. *J. Visualized Exp.* **2020**, No. 158, No. 10.3791/60888, DOI: 10.3791/60888.
(14) Wang, G.; McCain, M. L.; Yang, L.; He, A.; Pasqualini, F. S.; Agarwal, A.; Yuan, H.; Jiang, D.; Zhang, D.; Zangi, L.; et al. Modeling the mitochondrial cardiomyopathy of Barth syndrome with induced pluripotent stem cell and heart-on-chip technologies. *Nat. Med.* **2014**, *20* (6), 616−623.
(15) Ribeiro, A. J. S.; Ang, Y. S.; Fu, J. D.; Rivas, R. N.; Mohamed, T. M.; Higgs, G. C.; Srivastava, D.; Pruitt, B. L. Contractility of single cardiomyocytes differentiated from pluripotent stem cells depends on physiological shape and substrate stiffness. *Proc. Natl. Acad. Sci. U.S.A.* **2015**, *112* (41), 12705−12710.
(16) Bray, M.-A.; Sheehy, S. P.; Parker, K. K. Sarcomere alignment is regulated by myocyte shape. *Cell Motil. Cytoskeleton* **2008**, *65* (8), 641−651.
(17) Ribeiro, A. J. S.; Denisin, A. K.; Wilson, R. E.; Pruitt, B. L. For whom the cells pull: Hydrogel and micropost devices for measuring traction forces. *Methods* **2016**, *94*, 51−64.
(18) McCain, M. L.; Lee, H.; Aratyn-Schaus, Y.; Kléber, A. G.; Parker, K. K. Cooperative coupling of cell-matrix and cell-cell adhesions in cardiac muscle. *Proc. Natl. Acad. Sci. U.S.A.* **2012**, *109* (25), 9881−9886.
(19) Higgs, G. *Microsystems for Studying Single Heart Cell Mechanobiology*, Doctoral, Stanford University: 2013.
(20) Vite, A.; Radice, G. L. N-cadherin/catenin complex as a master regulator of intercalated disc function. *Cell Commun. Adhes.* **2014**, *21* (3), 169−179.
(21) Goncharova, E. J.; Kam, Z.; Geiger, B. The involvement of adherens junction components in myofibrillogenesis in cultured cardiac myocytes. *Development* **1992**, *114* (1), 173−183.
(22) Simpson, D. G.; Decker, M. L.; Clark, W. A.; Decker, R. S. Contractile activity and cell-cell contact regulate myofibrillar organization in cultured cardiac myocytes. *J. Cell Biol.* **1993**, *123* (2), 323−336.
(23) Wu, J. C.; Sung, H. C.; Chung, T. H.; DePhilip, R. M. Role of N-cadherin- and integrin-based costameres in the development of rat cardiomyocytes. *J. Cell. Biochem.* **2002**, *84* (4), 717−724.
(24) Chopra, A.; Tabdanov, E.; Patel, H.; Janmey, P. A.; Kresh, J. Y. Cardiac myocyte remodeling mediated by N-cadherin-dependent mechanosensing. *Am J Physiol Heart Circ Physiol.* **2011**, *300* (4), H1252−H1266.
(25) Chopra, A.; Patel, A.; Shieh, A. C.; Janmey, P. A.; Kresh, J. Y. α-Catenin Localization and Sarcomere Self-Organization on N-Cadherin Adhesive Patterns Are Myocyte Contractility Driven. *PLoS One* **2012**, *7* (10), No. e47592, DOI: 10.1371/journal.pone.0047592.
(26) Milani-Nejad, N.; Janssen, P. M. L. Small and large animal models in cardiac contraction research: Advantages and disadvantages. *Pharmacol. Ther.* **2014**, *141* (3), 235−249.
(27) Hasenfuss, G. Animal models of human cardiovascular disease, heart failure and hypertrophy. *Cardiovasc. Res.* **1998**, *39* (1), 60−76.
(28) Loh, C. Y.; Chai, J. Y.; Tang, T. F.; Wong, W. F.; Sethi, G.; Shanmugam, M. K.; Chong, P. P.; Looi, C. Y. The E-Cadherin and N-Cadherin Switch in Epithelial-to-Mesenchymal Transition: Signaling, Therapeutic Implications, and Challenges. *Cells* **2019**, *8* (10), 1118.
(29) Nag, K.; Adnan, N.; Kutsuzawa, K.; Akaike, T. *Cadherin-Fc Chimeric Protein-Based Biomaterials: Advancing Stem Cell Technology and Regenerative Medicine Towards Application*; Atwood, C.; Meethal, S. V., Eds.; 2014; pp 137−164.
(30) Collins, C.; Denisin, A. K.; Pruitt, B. L.; Nelson, W. J. Changes in E-cadherin rigidity sensing regulate cell adhesion. *Proc. Natl. Acad. Sci. U.S.A.* **2017**, *114* (29), E5835−E5844.
(31) Drees, F.; Reilein, A.; Nelson, W. J. Cell-Adhesion Assays. In *Cell Migration. Methods in Molecular Biology*, Guan, J. L., Ed.; Vol. *294*; Humana Press, 2005.
(32) Melero, C.; Kolmogorova, A.; Atherton, P.; Derby, B.; Reid, A.; Jansen, K.; Ballestrem, C. Light-Induced Molecular Adsorption of Proteins Using the PRIMO System for Micro-Patterning to Study Cell Responses to Extracellular Matrix Proteins. *J. Visualized Exp.* **2019**, No. 152, No. e60092, DOI: 10.3791/60092-v.
(33) Strale, P. O.; Azioune, A.; Bugnicourt, G.; Lecomte, Y.; Chahid, M.; Studer, V. Multiprotein Printing by Light-Induced Molecular Adsorption. *Adv. Mater.* **2016**, *28* (10), 2024−2029.
(34) Engler, A. J.; Carag-Krieger, C.; Johnson, C. P.; Raab, M.; Tang, H.-Y.; Speicher, D. W.; Sanger, J. W.; Sanger, J. M.; Discher, D. E. Embryonic cardiomyocytes beat best on a matrix with heart-like elasticity: scar-like rigidity inhibits beating. *J. Cell Sci.* **2008**, *121* (22), 3794−3802.
(35) Pardon, G.; Vander Roest, A. S.; Chirikian, O.; Birnbaum, F.; Lewis, H.; Castillo, E. A.; Wilson, R.; Denisin, A. K.; Blair, C. A.; Holbrook, C.; et al. Tracking single hiPSC-derived cardiomyocyte contractile function using CONTRAX an efficient pipeline for traction force measurement. *Nat. Commun.* **2024**, *15* (1), No. 5427, DOI: 10.1038/s41467-024-49755-3.
(36) Burridge, P. W.; Matsa, E.; Shukla, P.; Lin, Z. C.; Churko, J. M.; Ebert, A. D.; Lan, F.; Diecke, S.; Huber, B.; Mordwinkin, N. M.; et al. Chemically defined generation of human cardiomyocytes. *Nat. Methods* **2014**, *11* (8), 855−860.
(37) Zhao, B.; Zhang, K.; Chen, C. S.; Lejeune, E. Sarc-Graph: Automated segmentation, tracking, and analysis of sarcomeres in hiPSC-derived cardiomyocytes. *PLoS Comput. Biol.* **2021**, *17* (10), No. e1009443.
(38) Ribeiro, A. J. S.; Schwab, O.; Mandegar, M. A.; Ang, Y. S.; Conklin, B. R.; Srivastava, D.; Pruitt, B. L. Multi-imaging method to assay the contractile mechanical output of micropatterned human iPSC-derived cardiac myocytes. *Circ. Res.* **2017**, *120* (10), 1572−1583.
(39) Butler, J. P.; Tolic-Norrelykke, I. M.; Fabry, B.; Fredberg, J. J. Traction fields, moments, and strain energy that cells exert on their surroundings. *Am. J. Physiol.: Cell Physiol.* **2002**, *282* (3), C595−605.
(40) Pasqualini, F. S.; Agarwal, A.; O'Connor, B. B.; Liu, Q.; Sheehy, S. P.; Parker, K. K. Traction force microscopy of engineered cardiac tissues. *PLoS One* **2018**, *13* (3), No. e0194706.
(41) Wheelwright, M.; Win, Z.; Mikkila, J. L.; Amen, K. Y.; Alford, P. W.; Metzger, J. M. Investigation of human iPSC-derived cardiac myocyte functional maturation by single cell traction force microscopy. *PLoS One* **2018**, *13* (4), No. e0194909.
(42) Davis, J.; Davis, C. L.; Correll, N. R.; Makarewich, A. C.; Schwanekamp, A. J.; Moussavi-Harami, F.; Wang, D.; York, J. A.; Wu, H.; Houser, R. S.; et al. A Tension-Based Model Distinguishes Hypertrophic versus Dilated Cardiomyopathy. *Cell* **2016**, *165* (5), 1147−1159.
(43) Tang, X.; Tofangchi, A.; Anand, S. V.; Saif, T. A. A novel cell traction force microscopy to study multi-cellular system. *PLoS Comput. Biol.* **2014**, *10* (6), No. e1003631.
(44) Strimaityte, D.; Tu, C.; Yanez, A.; Itzhaki, I.; Wu, H.; Wu, J. C.; Yang, H. Contractility and Calcium Transient Maturation in the Human iPSC-Derived Cardiac Microfibers. *ACS Appl. Mater. Interfaces* **2022**, *14* (31), 35376−35388.
(45) Rodriguez, M. L.; Beussman, K. M.; Chun, K. S.; Walzer, M. S.; Yang, X.; Murry, C. E.; Sniadecki, N. J. Substrate Stiffness, Cell Anisotropy, and Cell-Cell Contact Contribute to Enhanced Structural and Calcium Handling Properties of Human Embryonic Stem Cell-Derived Cardiomyocytes. *ACS Biomater. Sci. Eng.* **2019**, *5* (8), 3876−3888.
(46) Gavard, J.; Lambert, M.; Grosheva, I.; Marthiens, V.; Irinopoulou, T.; Riou, J. F.; Bershadsky, A.; Mege, R. M. Lamellipodium extension and cadherin adhesion: two cell responses to cadherin activation relying on distinct signalling pathways. *J. Cell Sci.* **2004**, *117* (Pt 2), 257−270.
(47) Goding, J. W. Use of Staphylococcal Protein-a as an Immunological Reagent. *J. Immunol. Methods* **1978**, *20* (Apr), 241−253.
(48) Edelstein, A. D.; Tsuchida, M. A.; Amodaj, N.; Pinkard, H.; Vale, R. D.; Stuurman, N. Advanced methods of microscope control using muManager software. *J. Biol. Methods* **2014**, *1* (2), No. e10, DOI: 10.14440/jbm.2014.36.

(49) Hohenester, E. Structural biology of laminins. *Essays Biochem.* **2019**, *63* (3), 285−295.
(50) Jung, J. P.; Hu, D.; Domian, I. J.; Ogle, B. M. An integrated statistical model for enhanced murine cardiomyocyte differentiation via optimized engagement of 3D extracellular matrices. *Sci. Rep.* **2015**, *5*, No. 18705.
(51) Castillo, E. A. *Engineering the Microenvironment at the Protein-Hydrogel Interface to Investigate the Role of the Extracellular Matrix Protein Type in Single Cell Cardiomyocyte Structure and Function*, Doctoral, Stanford University: 2021.
(52) Denisin, A. K.; Pruitt, B. L. Tuning the Range of Polyacrylamide Gel Stiffness for Mechanobiology Applications. *ACS Appl. Mater. Interfaces* **2016**, *8* (34), 21893−21902.
(53) Van Vliet, K. J. Instrumentation and Experimentation. In *Handbook of Nanoindentation with Biological Applications*; Oyen, M. L., Ed.; Jenny Stanford Publishing, 2019; pp 39−76.
(54) Lin, D. C.; Horkay, F. Nanomechanics of polymer gels and biological tissues: A critical review of analytical approaches in the Hertzian regime and beyond. *Soft Matter* **2008**, *4* (4), 669−682.
(55) Roberts, B.; Haupt, A.; Tucker, A.; Grancharova, T.; Arakaki, J.; Fuqua, M. A.; Nelson, A.; Hookway, C.; Ludmann, S. A.; Mueller, I. A.; et al. Systematic gene tagging using CRISPR/Cas9 in human stem cells to illuminate cell organization. *Mol. Biol. Cell* **2017**, *28* (21), 2854−2874.
(56) Roberts, B.; Hendershott, M. C.; Arakaki, J.; Gerbin, K. A.; Malik, H.; Nelson, A.; Gehring, J.; Hookway, C.; Ludmann, S. A.; Yang, R.; et al. Fluorescent Gene Tagging of Transcriptionally Silent Genes in hiPSCs. *Stem Cell Rep.* **2019**, *12* (5), 1145−1158.
(57) Sharma, A.; Li, G.; Rajarajan, K.; Hamaguchi, R.; Burridge, P. W.; Wu, S. M. Derivation of highly purified cardiomyocytes from human induced pluripotent stem cells using small molecule-modulated differentiation and subsequent glucose starvation. *J. Visualized Exp.* **2015**, *2015* (97), 52628.
(58) Schindelin, J.; Arganda-Carreras, I.; Frise, E.; Kaynig, V.; Longair, M.; Pietzsch, T.; Preibisch, S.; Rueden, C.; Saalfeld, S.; Schmid, B.; et al. Fiji: an open-source platform for biological-image analysis. *Nat. Methods* **2012**, *9* (7), 676−682.
(59) Kandow, C. E.; Georges, P. C.; Janmey, P. A.; Beningo, K. A. Polyacrylamide Hydrogels for Cell Mechanics: Steps Toward Optimization and Alternative Uses. *Methods Cell Biol.* **2007**, *83* (07), 29−46.
(60) Schwarz, U. S.; Soine, J. R. Traction force microscopy on soft elastic substrates: A guide to recent computational advances. *Biochim. Biophys. Acta* **2015**, *1853* (11 Pt B), 3095−3104.
(61) Dembo, M.; Wang, Y. L. Stresses at the cell-to-substrate interface during locomotion of fibroblasts. *Biophys. J.* **1999**, *76* (4), 2307−2316.
(62) Kraning-Rush, C. M.; Carey, S. P.; Califano, J. P.; Reinhart-King, C. A. *Quantifying Traction Stresses in Adherent Cells*; Academic Press Inc., 2012; Vol. *110*, pp 139−178.
(63) Hansen, P. C.; O'Leary, D. P. The Use of the L-Curve in the Regularization of Discrete Ill-Posed Problems. *SIAM Journal on Scientific Computing* **1993**, *14* (6), 1487−1503.
(64) Kulkarni, A. H.; Ghosh, P.; Seetharaman, A.; Kondaiah, P.; Gundiah, N. Traction cytometry: regularization in the Fourier approach and comparisons with finite element method. *Soft Matter* **2018**, *14* (23), 4687−4695.

https://doi.org/10.1021/acsami.4c11934
ACS Appl. Mater. Interfaces 2025, 17, 174−186